Pergamon

Int. J. Mech. Sci. Vol. 38, No. 1, pp. 1–17, 1996
Elsevier Science Ltd

0020–7403/96 $9.50 + 0.00

0020–7403(95)00036–4

FINITE ELEMENT ANALYSIS OF THE RAKE ANGLE EFFECTS IN ORTHOGONAL METAL CUTTING

ALBERT J. SHIH

Process Engineering Center, Fuel Systems, Cummins Engine Co. Inc., Columbus, IN 47202-3005, U.S.A.

(*Received* 5 *July* 1994; *and in revised form* 27 *January* 1995)

Abstract—The plane-strain finite element method is developed and applied to model the orthogonal metal cutting of annealed low carbon steel with continuous chip formation. Four sets of simulation results for cutting with $-2°$, $0°$, $5°$, and $15°$ rake angle are summarized and compared to analyze the effects of rake angle in the cutting processes. The initial and deformed finite element meshes, as the cutting reaches steady-state condition, are first presented. Simulation results of the cutting forces and residual stresses, along with the X-ray diffraction measurements of the residual stresses generated using a worn cutting tool with $5°$ rake angle, are used to identify the influences of the rake angle and tool sharpness. Elements are selected to represent three sections along the shear and contact zones and under the cut surface. The normal and shear stresses, distributions of parameters along these three sections, and contours of temperature, plastic strain, and effective stress are then presented. Limitations of the finite element method for metal cutting simulation are discussed.

NOTATION

D_s	distance in the cutting direction between the node ahead of the tool tip and the face of the cutting tool
D_{sl}	distance limit in the element separation criterion
F_c	cutting force
F_f	feed force
F_r	resultant cutting force
t, t_c	depth of cut and chip thickness
Y_s	length of the sticking friction region
α	rake angle of the cutting tool
ϕ	shear angle
μ_{av}	averaged friction coefficient along the tool face
μ_d	friction coefficient in the sliding friction region
σ_n, σ_s	normal and shear stresses in the primary and secondary deformation zone

1. INTRODUCTION

The plane-strain orthogonal metal cutting process, with the direction of relative movement of the wedge-shaped cutting tool perpendicular to its straight cutting edge, has been extensively studied since it provides a reasonably good modeling of the chip formation on the major cutting edge of many metal removal processes such as turning, milling, drilling, grinding, etc. One of the important parameters in the orthogonal metal cutting process is the rake angle between the face of the cutting tool and the plane perpendicular to the cutting direction [1, 2]. The magnitude of rake angle has significant effects on the performance of the cutting tool and the integrity of the cut surface. The main objective of this research is to apply the finite element method to study the rake angle effects in orthogonal metal cutting of annealed AISI 1020 carbon steel with continuous chip formation. Finite element simulation results of the orthogonal metal cutting using four sets of perfectly sharp cutting tools with rake angles equal to $-2°$, $0°$, $5°$, and $15°$, respectively, are summarized to identify the differences and similarities of the deformation of the work-material. Another objective of this study is to investigate the initiation of discontinuous chip formation as the rake angle becomes smaller.

Based on the updated Lagrangian formulation, the finite element simulation of orthogonal metal cutting with zero or negative rake angle has difficulties in achieving the steady-state chip formation, especially in the initial stage of the cutting process. However, the finite element method based on the flow formulation has been successfully applied to analyze the metal cutting with negative rake angle [3,4]. A finite element technique is developed to gradually decrease the rake angle and increase the coefficient of friction to the designated values during the initial stage of the cutting process and then continue the movement of the cutting tool until the steady-state chip formation is achieved.

The residual stresses on the cut surface is an important factor in determining the performance and fatigue strength of mechanical components. The finite element method has been developed and applied to predict the distributions of residual stresses in orthogonal metal cutting using a worn high speed steel cutting tool with 5° rake angle and the numerical analysis results, compared to the X-ray diffraction measurements, has also shown good agreement [5, 6]. The same unloading and cooling procedures [5] are applied in this study to predict the distributions of residual stresses under the cut surface due to orthogonal metal cutting with four different rake angles.

In this paper, the finite element modeling and techniques are first introduced. Detailed finite element simulation results, including the design of initial finite element meshes, deformed meshes as the cutting reaches steady-state condition, cutting forces, distributions of residual stresses under the cut surface, distributions of normal and shear stresses, distributions of parameters along the shear and contact zones and under the cut surface, and contours of temperature, plastic strain, and effective stress, are then presented and compared to gain better understanding of the rake angle effects in orthogonal metal cutting.

2. FINITE ELEMENT MODELING AND TECHNIQUES

The thermal elastic–viscoplastic finite element formulation has been developed and implemented to model the large strain and high strain-rate plastic deformation in the shear or primary deformation zone and the contact, friction, and heat generation along the contact or secondary deformation zone between the chip and cutting tool [5–7]. To cope with the geometrical and material nonlinearities, the finite element simulation is carried out incrementally. Detailed mathematical expressions, flowchart, and material properties for the finite element formulation have been summarized in Refs [6, 7] and are omitted in this paper.

In the past decade, several finite element techniques have been developed for more accurate and efficient modeling of metal cutting. Some of the milestones achieved are summarized as follows: element separation for chip formation modeling [8], element separation criteria [7–9], tool wear modeling [7–9], mesh rezoning [7], and unloading and cooling for residual stresses prediction [5].

Friction along the tool/chip contact interface during the cutting process is a very complicated phenomenon. Cutting experiments showed that the friction can be divided into sticking and sliding friction regions [2,10]. A sticking-sliding friction modeling [6] has been developed. Two different models are used to calculate the friction forces in the sticking and sliding regions. In the sticking friction region, the friction force along the boundary of an element in contact with the tool face is obtained by multiplying the maximum shear stress, k, and contact length of the element. The Coulomb friction law is applied in the sliding friction region. Two parameters are needed in this friction modeling, i.e. the length of the sticking friction region, Y_s, and the coefficient of friction in the sliding friction region, μ_d.

The friction forces and magnitude of these two parameters are influenced by the types of tool and work material, tool wear, coating, chip breaker, rake angle, cutting speed, depth of cut, coolant, coolant pressure, etc. For most of the cutting processes, both parameters are still lacking experimental data base to support the numerical analysis. Y_s can be estimated by the wear pattern of the cutting tool [6, 10]. In the experiments of metal cutting of annealed AISI 1020 carbon steel using a worn high speed steel cutting tool with 5° rake angle [5, 6], the value of Y_s was measured using the microscope and estimated to be 65 μm. The value for μ_d, under the temperature, pressure, lubrication, and speed in the sliding

friction region, is set to 0.14. The estimated $Y_s = 65$ μm and $\mu_d = 0.14$, same as the values used in the previous study in Refs [5, 6], are used for all four cutting configurations. The assumption of Y_s and μ_d being independent of the rake angle simplifies the modeling and isolates the rake angle as the only variable in the finite element simulation.

The instability during iterations to achieve equilibrium in the initial stage of the cutting process may occur due to large element distortion. For cutting tools with zero or negative rake angle, this phenomenon is more significant. The approach used in this study to initiate a steady-state cutting process is to start the incremental movement of an assumed friction-less cutting tool with the same or larger rake angle in the initial stage of the cutting process, then gradually reduce the rake angle and increase Y_s and μ_d to the desired values as the cutting tool moves forward. The cutting tool must continue the movement under the desired cutting condition for a distance long enough, at least twenty times the depth of cut, to ensure the steady-state chip formation is achieved.

The element separation criterion is based on distance [5]. Elements in front of the cutting tool separate when the distance in the cutting direction between the face of the cutting tool and the node in front of the tool tip is smaller than a given value D_{sl}. In this study, D_{sl} is set at 4 μm for all four cutting operations.

3. FINITE ELEMENT ANALYSIS OF THE RAKE ANGLE EFFECTS

Four sets of finite element simulation results with rake angles equal to $-2°$, $0°$, $5°$, and $15°$ are presented and summarized to identify the rake angle effects in the orthogonal metal cutting of annealed AISI 1020 carbon steel with continuous chip formation. The tool material is high speed steel, depth of cut is 101.6 μm (0.004 in.), and cutting speed is 584.2 mm/s.

3.1. *Initial finite element meshes*

The initial finite element meshes, configuration of the cutting tools, definition of the rake angle, α, and dimensions of the elements are shown in Fig. 1. Ten layers of elements, 10.16 μm in height are used to model the chip formation. Under the cut surface, four layers of elements, 2.54 μm in height and another four layers, 5.08 μm in height are used to get a good prediction of the distributions of residual stresses. Two major differences of these two finite element meshes are the width of undeformed elements and the inclination or offset of elements in the tenth layer. The offset of elements in the tenth layer is 80.8 μm for $\alpha = -2°$ and $0°$ and 50.8 μm for $\alpha = 5°$ and $10°$. The width of undeformed elements is 70 μm for $\alpha = -2°$ and $0°$ and 35 μm for $\alpha = 5°$ and $10°$. Some trial and error simulation runs are necessary to find the suitable values of these two important parameters for cutting with different rake angles, which is a very challenging part of this research. For example, if the finite element mesh for $\alpha = 5°$ [Fig. 1(b)] is applied to the simulation using a cutting tool with $\alpha = 0°$, the divergence problem during numerical iterations to achieve equilibrium condition will occur due to excess element distortion. The design of a good initial finite element mesh affects not only the stability in the numerical analysis but also the accuracy of the simulation results.

3.2. *Deformed finite element meshes*

As the cutting tool proceeds, the mesh rezoning technique is applied to add, refine, combine, and delete columns of elements in front of and behind the cutting tool until the steady-state chip formation is achieved [5]. Four deformed finite element meshes during the steady-state chip formation, for $\alpha = -2°$, $0°$, $5°$, and $15°$, are illustrated in Fig. 2. The enlarged view of the deformed meshes near the cutting tool is shown in Fig. 3. Comparing these deformed finite element meshes, the effect of rake angle to the distortion of elements or deformation of work-material is obvious. The most severe shear distortion of elements can be seen in the contact zone for cutting with $\alpha = -2°$. This also demonstrates why the width of undeformed elements is 70 μm for $\alpha = -2°$ instead of 35 μm for $\alpha = 5°$, as shown in Fig. 1. Under the cut surface, the cutting with smaller rake angle generates more significant distortion of elements. In the following sections, the distributions of residual stresses, plastic strain, temperature, etc. also validate this observation.

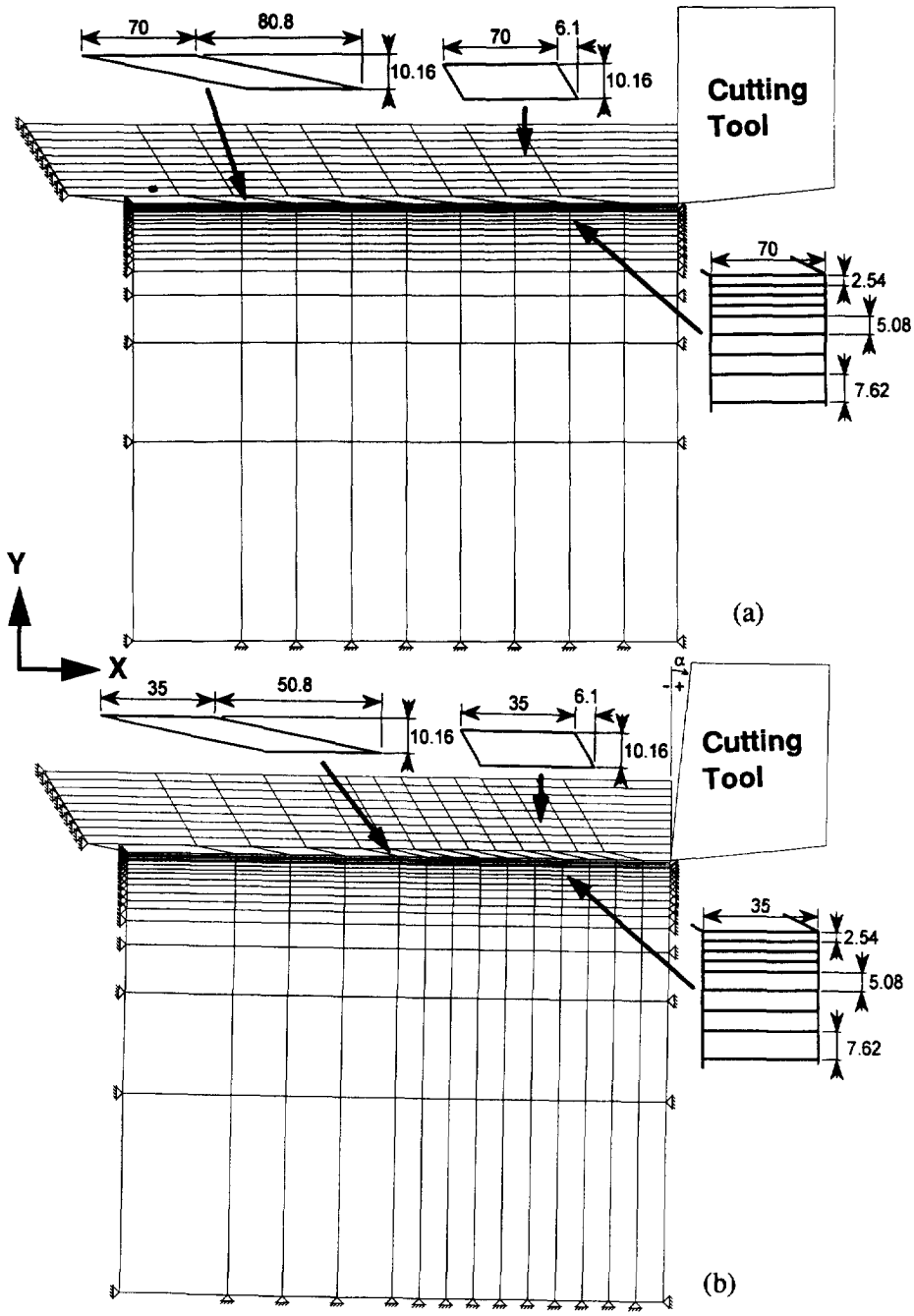

Fig. 1. The initial finite element meshes and the definition of rake angle α, (a) initial finite element mesh for $\alpha = -2°$ and $0°$, (b) initial finite element mesh for $\alpha = 5°$ and $15°$.

In Fig. 3, three sections of elements are selected to represent: 1. the shear zone (elements S1–S10), 2. the contact zone (elements C1–C20 for $\alpha = -2°$, C1–C15 for $\alpha = 0°$ and $5°$, and C1–C9 for $\alpha = 15°$), and 3. the cut surface (elements D1–D11). These elements will be used later to show the distributions of normal and shear stresses and other parameters along these three sections.

The chip thickness, contact length, cutting ratio, and shear angle, obtained from the four deformed finite element meshes in Fig. 3, are listed in Table 1. The depth of cut (t), chip thickness (t_c), and rake angle (α) are used to calculate the shear angle, ϕ:

$$\phi = \arctan\left(\frac{\cos\alpha}{t_c/t - \sin\alpha}\right). \tag{1}$$

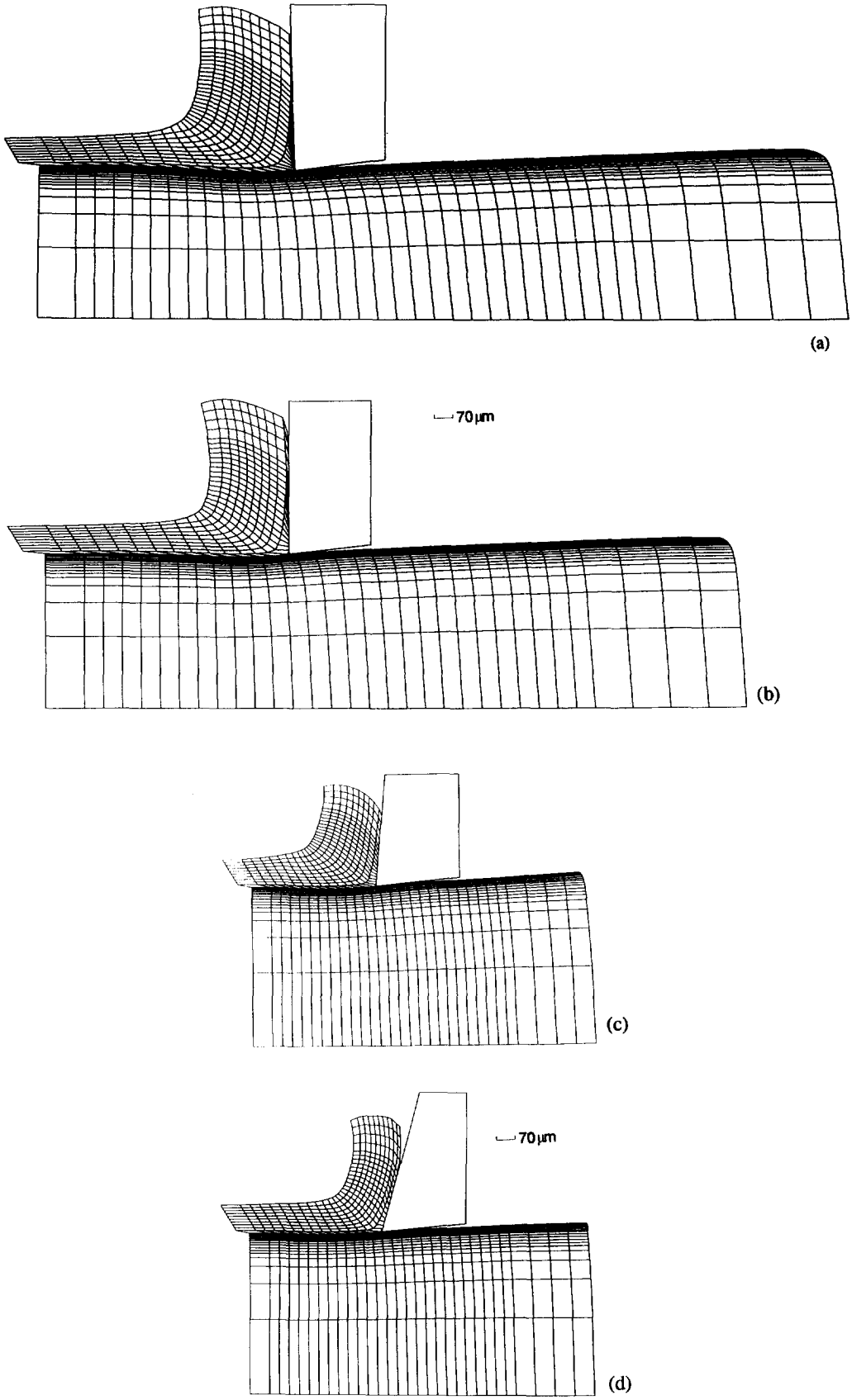

Fig. 2. Deformed finite element meshes during steady-state orthogonal metal cutting processes, (a) $\alpha = -2°$, (b) $\alpha = 0°$, (c) $\alpha = 5°$, (d) $\alpha = 15°$.

Thicker chip, smaller shear angle, and longer contact length can be seen using the cutting tool with smaller rake angle. Table 1 also summarizes the values of the maximum temperature, plastic strain, plastic strain-rate, effective stress, yield stress, and hydrostatic stress and minimum hydrostatic stress within the workpiece. Cutting with $\alpha = -2°$ generates the most severe distortion of elements and the highest values of the maximum temperature, plastic strain, plastic strain-rate, effective stress, yield stress, and hydrostatic stress. It is interesting that the highest value of the maximum plastic strain-rate is generated by cutting with 5° rake angle.

In this study, fracture is not included in the material modeling. Most of the chips involve some fracture due to the large plastic strain and high strain-rate. Compared to the pictures of chip formation in cutting experiments, the curvature at the intersection of chip and free surface should be smaller and the shear band should be narrower. These discrepancies can be contributed to the lack of fracture or damage modeling in the finite element formation.

3.3. *Cutting forces*

The cutting and feed forces, F_c and F_f listed in Table 1, are the average of forces at each incremental step when the cutting tool moves twice the width of the uncut elements, i.e. 140 μm for $\alpha = -2°$ and 0° and 70 μm for $\alpha = -5°$ and 15°. The resultant force, F_r, is also

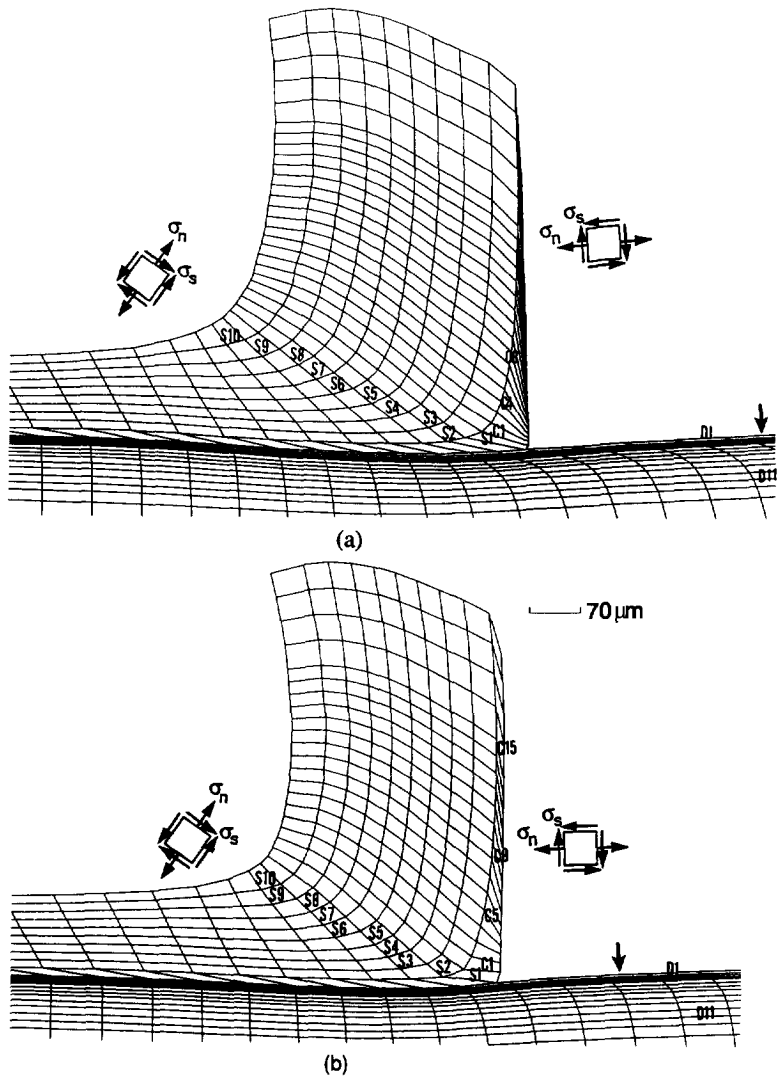

Fig. 3. Enlarged view of the deformed finite element meshes near the cutting tool and the selected elements along the shear zone (S), contact zone (C), and cut surface (D), (a) $\alpha = -2°$, (b) $\alpha = 0°$, (c) $\alpha = 5°$, (d) $\alpha = 15°$.

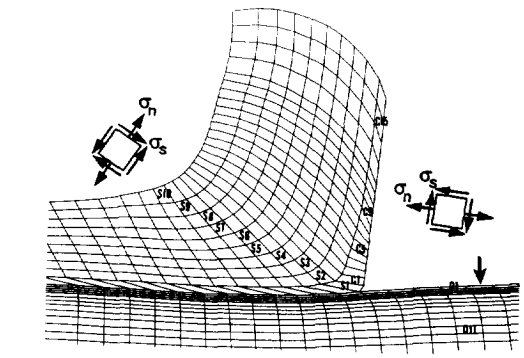

(c)

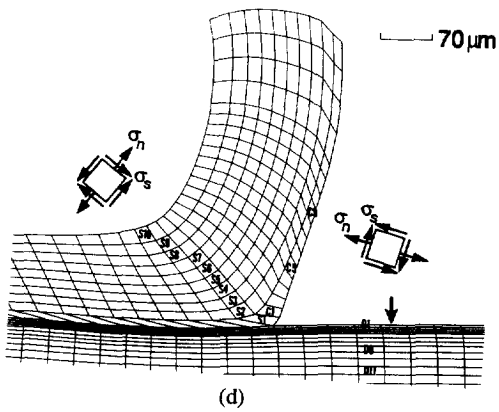

(d)

Fig. 3. (*Contd.*)

Table 1. Summary of the rake angle effects in orthogonal metal cutting

	(Rake angle deg)			
	−2	0	5	15
Depth of cut, t (μm)	101.6	101.6	101.6	101.6
Chip thickness, t_c	333	293	210	168
Cutting ratio (t/t_c)	0.305	0.347	0.484	0.605
Shear angle ϕ (deg)	16.8	19.1	26.7	34.7
Contact length (μm)	378	363	259	186
Max. temperature (°C)	830	799	730	616
Max. plastic strain	6.19	4.43	3.18	2.58
Max. plastic strain rate (s^{-1})	5140	6980	7990	6500
Max. effective stress (MPa)	3250	2670	2590	2200
Max. yield stress (MPa)	994	977	960	884
Max. hydrostatic stress (MPa)	598	422	351	297
Min. hydrostatic stress (MPa)	−1190	−1020	−1010	−948
Averaged cutting force F (N/mm)	585	452	445	243
Averaged feed force F_f (N/mm)	173	150	148	34
Resultant force F_r (N/mm)	603	476	468	245
μ_{av}	0.25	0.33	0.42	0.42

listed in Table 1. The lower the rake angle, the higher the cutting, feed, and resultant forces can be seen.

The resultant force can be decomposed into forces normal and parallel to the face of the cutting tool. The ratio of the magnitude of these two forces is defined as μ_{av}, the averaged

coefficient of friction between the chip and cutting tool. μ_{av} listed in Table 1, ranges from 0.25 for $\alpha = -2°$ to 0.42 for $\alpha = 15°$. For such a work-material, all values should be higher. This represents μ_d should be higher than 0.14. The reason μ_{av} is lower for $\alpha = -2°$ is because it has longer tool/chip contact length which makes the contribution of friction force in the sliding region more significant.

The impact of higher μ_d to the finite element simulation can be predicted. Higher μ_d will result in longer contact length and larger shear distortion of elements, especially in the sliding friction region. For cutting with $\alpha = 15°$, the deformed elements in the secondary deformation zone show μ_d can be further increased because the distortion of elements is not as severe as the other three cutting configurations. However, as shown in Fig. 3(a), it will be difficult to increase the μ_d for cutting with $\alpha = -2°$ because elements in the sliding region have been severely distorted and instability during iterations to achieve equilibrium may very likely happen.

3.4. *Distributions of residual stresses*

The X-ray diffraction method and chemical etching technique were applied to measure the distributions of residual stresses under the cut surface of the AISI 1020 carbon steel workpiece using the worn high speed steel cutting tool with 5° rake angle. Under nominally the same cutting condition, the finite element method was applied to predict the distributions of residual stresses [5, 6]. The finite element predictions of the distributions of residual stresses under the cut surface, along columns of elements marked by four arrow symbols in Fig. 3, are shown in Fig. 4. The X-ray diffraction measurements and finite element predic-

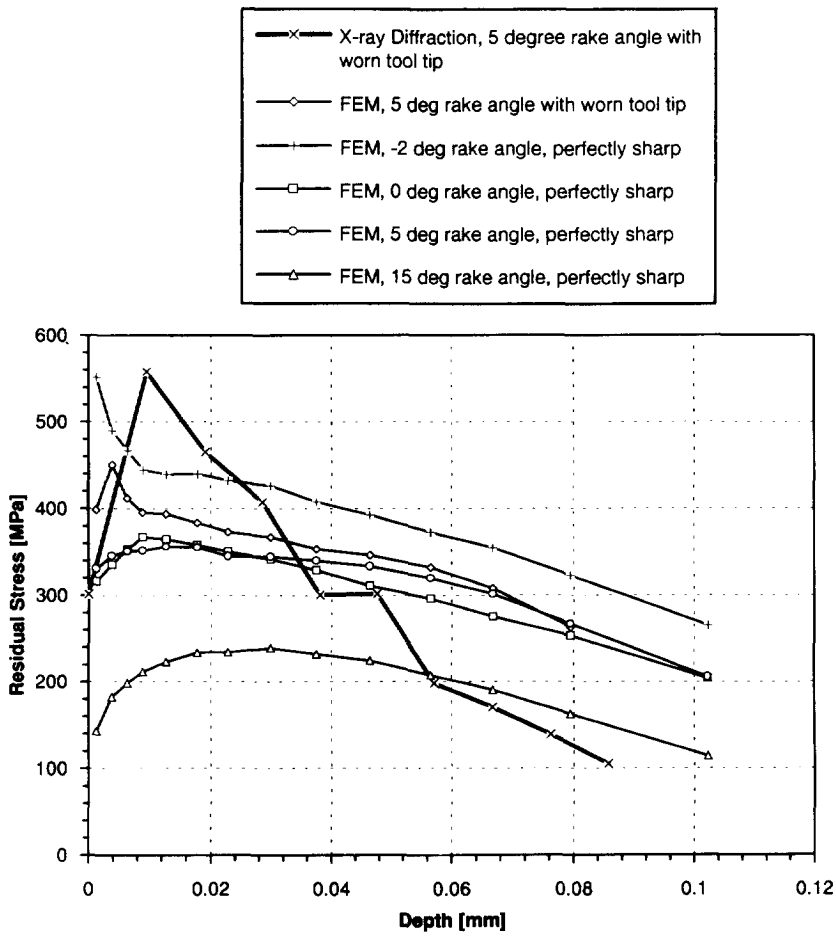

Fig. 4. The distributions of the residual stresses in the cutting direction for $\alpha = -2°$, 0°, 5°, and 15°, and the comparison with X-ray diffraction measurement and finite element simulation of residual stresses using the worn cutting tool with 5° rake angle.

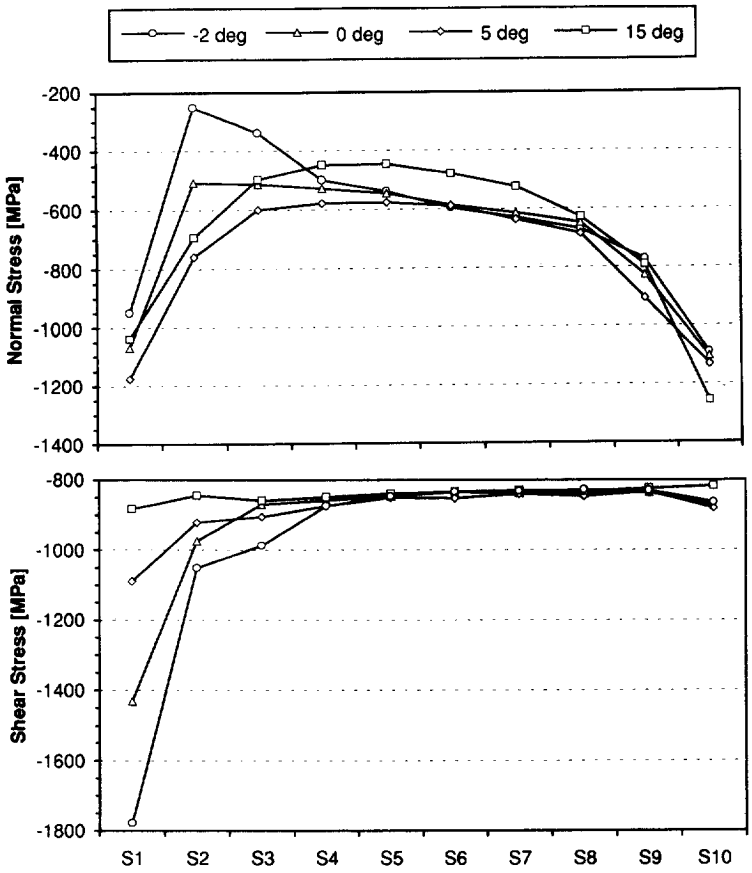

Fig. 5. The distributions of normal and shear stresses along the shear (primary deformation) zone.

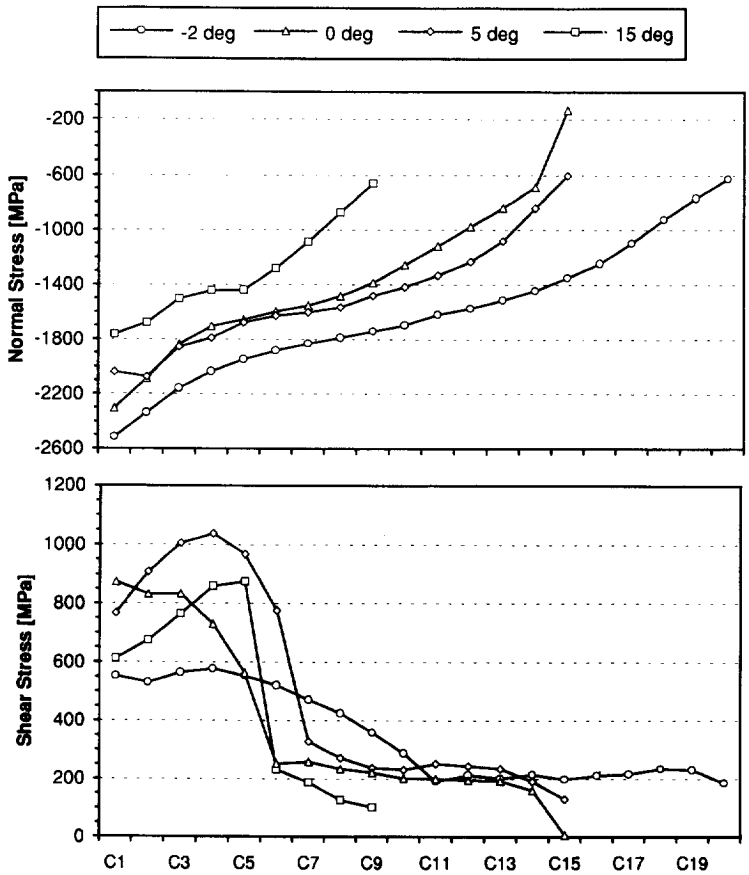

Fig. 6. The distributions of normal and shear stresses along the contact (secondary deformation) zone.

tions of the distributions of residual stresses using the worn cutting tool with 5° rake angle are also presented in Fig. 4 for mutual comparison.

The effects of worn cutting tool and rake angle to the distributions of residual stresses can be identified. The perfectly sharp cutting tool with $\alpha = 5°$ generates slightly lower (about 80 MPa less on the cut surface) and smoother tensile residual stresses near the cut surface relative to the residual stresses generated by the worn cutting tool with the same rake angle. Residual stresses generated by the perfectly sharp cutting tool with $\alpha = 0°$ and 5° are about the same in both magnitude and pattern of distribution (both start from 320 MPa, reach the peak of 360 MPa about 10 μm under the cut surface, and gradually reduce to zero or compressive residual stresses inside the workpiece). Relatively low tensile residual stresses, starts from 140 MPa on the cut surface and reaches the peak of 240 MPa 30 μm under the cut surface, can be seen for $\alpha = 15°$. For $\alpha = -2°$, very severe distortion of elements on the cut surface and relatively high tensile residual stresses (550 MPa on the cut surface and gradually decays to 260 MPa 100 μm under the cut surface) can be seen. The location of the peak of high tensile residual stress for $\alpha = -2°$ is on the cut surface, which is different from the other residual stresses distributions.

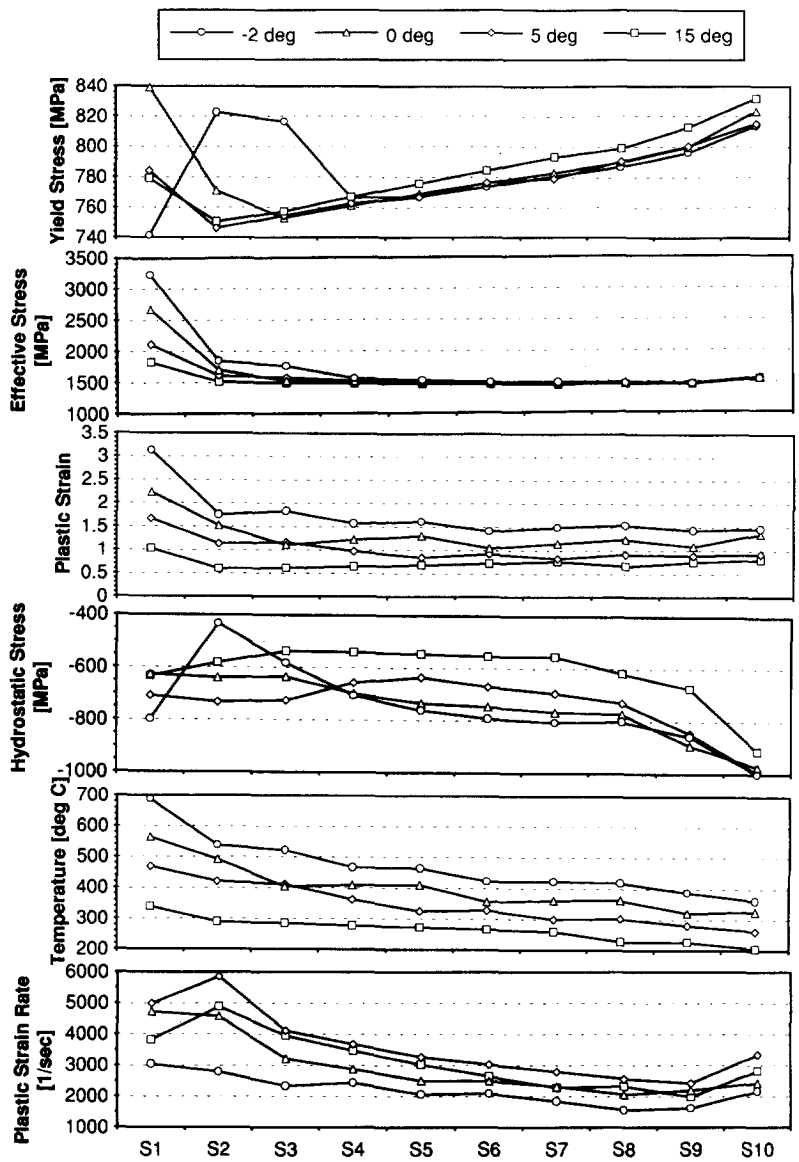

Fig. 7. The distributions of yield stress, effective stress, plastic strain, hydrostatic stress, temperature, and plastic strain-rate along the shear (primary deformation) zone.

3.5. *Distributions of the normal and shear stresses*

The averaged element stress tensors in the shear zone (elements S1–S10 in Fig. 3) are transformed by rotating an angle, which is equal to the magnitude of the shear angle ϕ (16.8°, 19.1°, 26.7°, and 34.7° for $\alpha = -2°$, 0°, 5°, and 15°, respectively), in the c.w. direction to get the normal and shear stresses (represented by symbols σ_n and σ_s in Fig. 3). Similarly, the averaged element stress tensors in the contact zone are transformed by rotating an angle equal to the magnitude of the rake angle in the c.w. direction to calculate the normal and shear stresses. The finite element predictions of the distributions of normal and shear stresses along the shear and contact zones are shown in Figs 5 and 6, respectively.

Compressive normal stresses can be seen across the shear zone. High compressive normal stresses (950–1250 MPa) occur at both ends of the shear zone (elements S1 and S10). Low compressive normal stresses (− 250 MPa at S2, − 500 MPa at S2, − 570 MPa at S5, and − 450 MPa at S5 for $\alpha = -2°$, 0°, 5°, and 15°, respectively) appear either near the tool tip (S2) or in the middle of the shear zone (S5). The distributions of shear stresses show a similar trend: peaks of high shear stress (− 1780, − 1440, − 1090, and − 880 MPa at

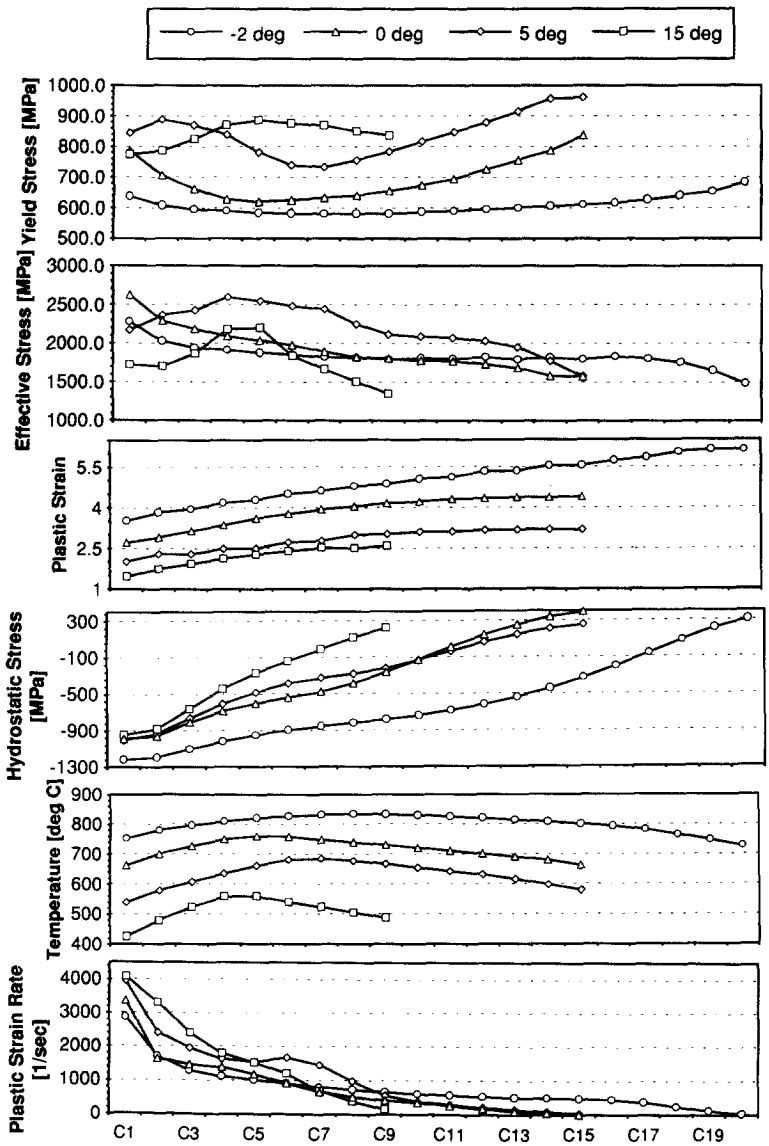

Fig. 8. The distributions of yield stress, effective stress, plastic strain, hydrostatic stress, temperature, and plastic strain-rate along the contact zone (secondary deformation zone).

$\alpha = -2°$, 0°, 5°, and 15°, respectively) appear in front of the tool tip, S1, and the values increase to a fairly constant level at about -850 to -880 MPa between S4 and S10.

Depending on the contact length, width of the undeformed mesh, and distortion of elements, the number of elements in contact along the tool/chip interface varies in four cutting configurations. The normal stresses along the tool/chip contact zone, as shown in Fig. 6, exhibit a similar trend of distribution. High compressive normal stresses occur in front of the tool tip, C1 (-2500, -2300, -2050, -1750 MPa for $\alpha = -2°$, 0°, 5°, and 15°, respectively). The normal stresses then gradually decrease to near zero at the position where the chip starts to lose contact with the cutting tool. The high friction forces in the sticking friction region can be seen. Relatively low shear stresses appear in the sliding friction region. Cutting with $\alpha = 15°$ shows the shortest contact length (see Table 1), lowest normal stress, and fewest elements in contact among all four cutting conditions.

3.6. *Distributions of parameters under the cut surface and along the shear and contact zones*

The distributions of parameters along the shear zone are shown in Fig. 7. Three of the six parameters, i.e. effective stress, plastic strain, and temperature, show four levels of distribu-

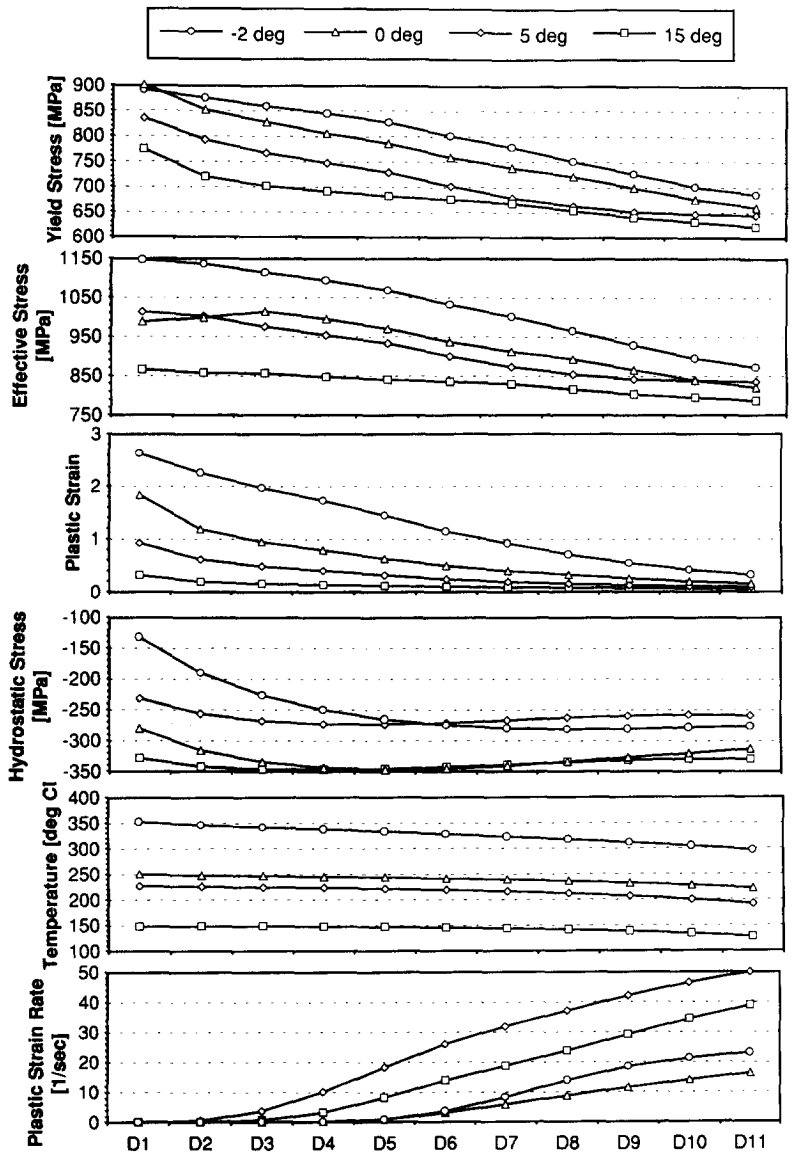

Fig. 9. The distributions of yield stress, effective stress, plastic strain, hydrostatic stress, temperature, and plastic strain-rate under the cut surface.

tions at four rake angles. These three parameters also show similar pattern of distributions: the peak values occur in front of the tool tip at S1 and then gradually decrease to a lower level from S4 to S10. The magnitude of yield stress is determined by the combination of strain hardening and temperature softening effects. For $\alpha = 0°$, 5° and 15°, high yield stresses occur at both ends of the shear zone (S1 and S10). For $\alpha = -2°$, the yield stresses show different pattern of distribution due to the high temperature induced low yield stress at element S1 (740 MPa at 695°C). Hydrostatic stresses in the shear zone are all compressive. High compressive hydrostatic stresses can be seen at S10 (900–1000 MPa). This phenomenon is similar to the high compressive hydrostatic stresses near the surface during the plastic bending of a beam. The region with high tensile hydrostatic stress indicates the possibility of incipient of cracks to start the discontinuous chip formation. The peak of high hydrostatic stress (− 420 MPa) at element S2 for $\alpha = -2°$ shows the tendency. High plastic strain-rate appears near the tool tip (S1 and S2) and while cutting with $\alpha = 5°$.

Figure 8 shows the distributions of parameters along the tool/chip contact zone. Due to the temperature softening effect, low yield stress for $\alpha = -2°$ can be seen, and the valleys of the distributions of yield stresses for $\alpha = -2°$, 0°, and 5° occur in the sliding friction region, i.e. 590 MPa at C8, 620 MPa at C5, and 740 MPa at C7 for $\alpha = -2°$, 0° and 5°, respectively. The peaks of temperature distributions, 830, 760, and 680°C, can also be identified at these three elements. For $\alpha = 15°$, the trend to distribution of yield stresses is just opposite to the other three curves because the temperature softening effect is relatively insignificant (under 550°C). Higher effective stresses can be seen along the contact zone than those in the shear zone (Fig. 7). Four levels of the distributions of plastic strain and temperature at different rake angles can be seen in the contact zone. Element with the highest plastic strain occurs in the contact zone where it starts to lose contact with the cutting tool. The values of maximum plastic strain in Fig. 8 (6.2, 4.4, 3.2, and 2.6 for $\alpha = -2°$, 0°, 5°, and 15°, respectively) match the values listed in Table 1. Transition of the hydrostatic stress from high compressive near the tool tip, from − 1200 to − 1000 MPa at C1, to tensile in the sliding friction region can be seen. High plastic strain-rate appears for $\alpha = 15°$ in the sticking friction region and for $\alpha = 5°$ in the sliding friction region.

Figure 9 shows the distributions of parameters under the cut surface. The cutting tool with $\alpha = -2°$ generates high yield stress, effective stress, plastic strain, and temperature. High plastic strain-rate and compressive hydrostatic stress can be seen for $\alpha = 5°$ and 15°, respectively. Comparing with the effective stress, hydrostatic stress, temperature, and plastic strain-rate in the shear and contact zones (Figs 7 and 8), relatively low values occur under the cut surface. Again, the high plastic strain-rate occurs while cutting with $\alpha = 5°$.

3.7. *Contours of temperature, plastic strain, and effective stress*

The contours of temperature, plastic strain, and effective stress during the steady-state cutting condition are shown in Figs 10–12. The contour plots, along with the data in Table 1 and Figs 7–9, are very helpful to get an overall picture of the distributions of parameters. Contour plots in Fig. 10 show similar pattern of temperature distributions for four different cutting configurations. The high temperature regions along the tool/chip interface appear in the sliding friction region, where the rate of heat generated due to friction and plastic work is equal to the rate of heat conducted into the chip and tool. Cutting with smaller rake angle also exhibits higher temperature gradient near the tool tip.

Figure 11 shows the contours of plastic strain during steady-state cutting process. The variation in rake angle significantly changes the magnitude of the plastic strain, however, the pattern of distribution remains the same. The value of plastic strain gradually increases as the work-material deforms while passing the shear zone and then the contact zone. The peak values of plastic strain distributions appear in the end of the sliding friction region where the elements start to lose contact with the cutting tools.

The effective stress contours during steady-state cutting process are shown in Fig. 12. Mesh rezoning has changed the values of effective stresses near the top of the chip. Cutting with $\alpha = 15°$ shows the contours of high effective stresses (region 7) spread along the contact zone. While cutting with smaller rake angle, the area of high effective stresses (regions 7 and 8) has moved toward the tool tip and also penetrates deeper inside the workpiece.

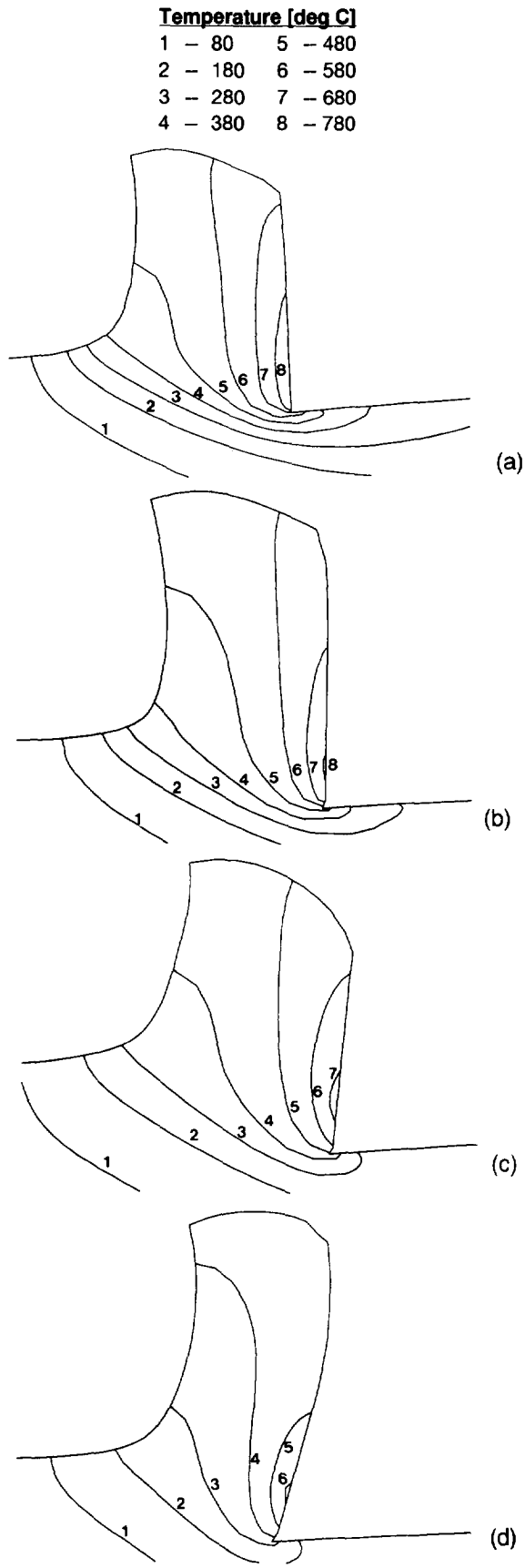

Fig. 10. Temperature contours during steady-state orthogonal cutting process, (a) $\alpha = -2°$, (b) $\alpha = 0°$, (c) $\alpha = 5°$, (d) $\alpha = 15°$.

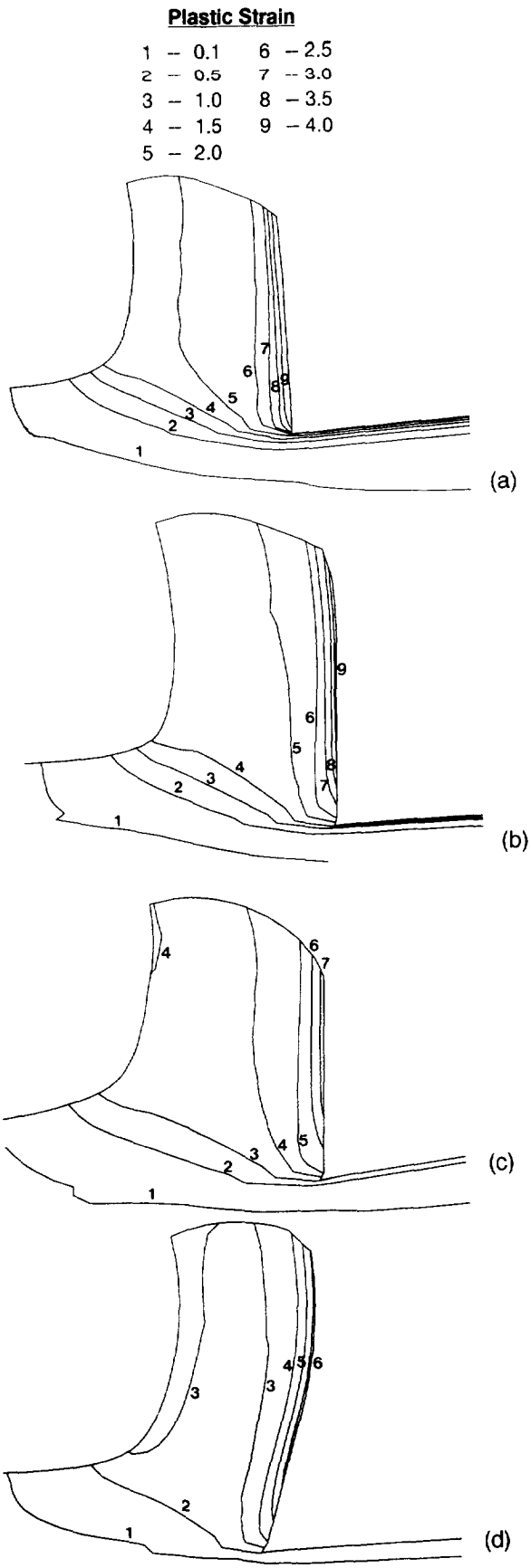

Fig. 11. Plastic strain contours during steady-state orthogonal cutting process, (a) $\alpha = -2°$, (b) $\alpha = 0°$, (c) $\alpha = 5°$, (d) $\alpha = 15°$.

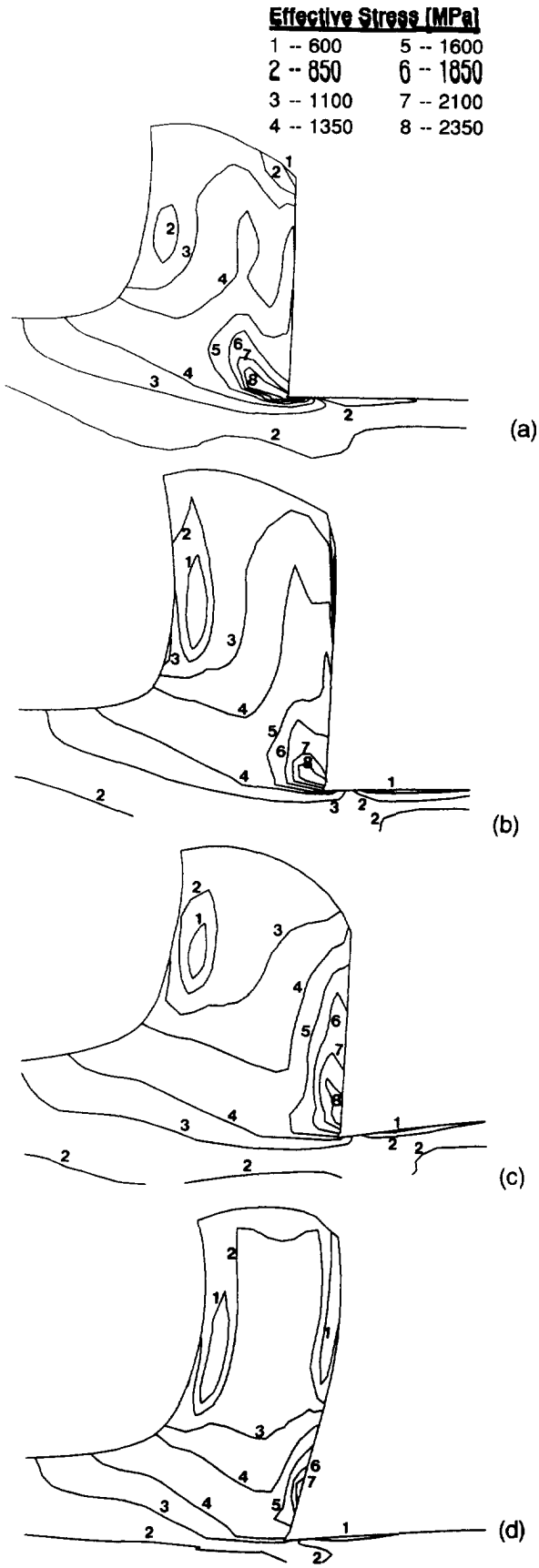

Fig. 12. Effective stress contours during steady-state orthogonal cutting process, (a) $\alpha = -2°$, (b) $\alpha = 0°$, (c) $\alpha = 5°$, (d) $\alpha = 15°$.

4. CONCLUDING REMARKS

In this paper, a large-strain finite element simulation program was developed and applied for the numerical analysis of orthogonal metal cutting using perfectly sharp cutting tools for four different rake angles. The initial and deformed finite element meshes and cutting forces were presented. The distributions of residual stresses under the cut surface were compared and analyzed. Distributions of normal and shear stresses, contours, and distributions of parameters along the contact and shear zones and under the cut surface were also presented and discussed.

The deformed finite element meshes in Fig. 3 suggested the modeling of work-material used in this study, which included the large strain, temperature, and strain-rate effects, was still not adequate. The modeling of fracture or damage of the work-material must be added especially for the cutting with small rake angle. The average coefficient of friction μ_{av} in Table 1 recommended that $\mu_d = 0.14$ was too low. We also concluded the increase of μ_d will have less impact to the cutting with larger rake angle. However, it will be very sensitive for cutting with zero or negative rake angle.

Several trial runs of the finite element simulation with more negative rake angle were conducted. It was interesting to see that, under the same cutting set-up and friction condition, the steady-state continuous chip formation could not be achieved while cutting with $-5°$ rake angle. The instability of the work-material may be originated by the large deformation of elements and the combination of temperature softening and strain and strain-rate hardening effects. The actual causes are still under study.

REFERENCES

1. M. C. Shaw, *Metal Cutting Principles*, p. 3. Oxford University Press, Oxford (1984).
2. G. Boothroyd and W. A. Knight, *Fundamentals of Machining and Machine Tools*, 2nd Ed., p. 76. Marcel Dekker, New York (1989).
3. J. T. Carroll III and J. S. Strenkowski, Finite element models of orthogonal cutting with application to single point diamond turning. *Int. J. Mech. Sci.* **30**, 899 (1988).
4. K. F. Eldridge, O. W. Dillon and W. Y. Lu, Thermo-viscoplastic finite element modeling of machining under various cutting conditions. *Trans. NAMRC* **XIX**, 162 (1991).
5. A. J. Shih and H. T. Yang, Experimental and finite element predictions of residual stresses due to orthogonal metal cutting. *Int. J. Num. Methods in Engng* **36**, 1487 (1993).
6. A. J. Shih, Finite element simulation of orthogonal metal cutting. *ASME. J. Engng for Ind.* **117**, (1995).
7. A. J. Shih, S. Chandrasekar and H. T. Yang, Finite element simulation of metal cutting process with strain-rate and temperature effects in *Fundamental Issues in Machining* (edited by B. E. Klamecki and K. J. Wienmann), Vol. 43, p. 11. ASME PED (1990).
8. J. S. Strenkowski and J. T. Carroll III, Finite element model of orthogonal metal cutting. *ASME J. Engng for Ind.* **107**, 349 (1985).
9. K. Komvopoulos and S. A. Erpenbeck, Finite element modeling of orthogonal metal cutting. *ASME J. Engng for Ind.* **113**, 253 (1991).
10. E. M. Trent, *Metal Cutting*, p. 27. Butterworth-Heinemann, Oxford (1991).